A refined spectral element model for wave propagation in multiscale hybrid epoxy/carbon fiber/graphene platelet composite shells

Fenfei Hua[1,2], Wanbiao Fu[1,2], Qingquan You[1,2], Qingyang Huang[1,2],

Farhad Abad[3], Xiaoqiang Zhou[1,2*]

[1]Department of Mechanics, School of Aerospace Engineering, Huazhong University of Science and Technology, Wuhan 430074, China

[2]Hubei Key Laboratory of Engineering Structural Analysis and Safety Assessment, Wuhan 430074, China

[3]Department of Naval Architecture, Ocean and Marine Engineering, University of Strathclyde, Glasgow G4 0LZ, UK

*Corresponding author: Dr. Xiaoqiang Zhou

E-mail: zhou_xq@hust.edu.cn

Abstract:

The propagation of elastic waves in heterogeneous media is of interest for impact dynamics and non-destructive detection. This work presents a refined spectral element model (RSEM) to study the wave propagation in multiscale hybrid composite (MHC) shells subjected to impulsive loadings. The doubly-curved MHC shell consists of epoxy, carbon fibers, and graphene platelets (GPLs). The GPLs are functionally distributed along the thickness of the shell. For the three-phase MHC, the Halpin-Tsai micromechanical model in conjunction with the Mori-Tanaka approach is exploited to determine the effective material properties. In the framework of four-variable shear deformation theory, the governing equations along with the natural boundary conditions are derived using Hamilton's principle. A two-node spectral shell element is developed according to the closed-from solutions. The accuracy of the RSEM is verified by comparison with published results in aspects of the natural frequency and transient responses. The wave dispersion characteristics, including the wave number, phase velocity, and group velocity are examined. In the context of high frequency and short wavelength, the proposed RSEM achieves high computational efficiency benefiting from its independence of mesh structure. The time domain responses clearly indicate the wave-boundary interactions, e.g., wave reflection, dispersion, and interference. It is revealed that the present model can well capture the fundamental wave modes of the MHC shell. Moreover, the inclusion of GPLs plays a significant role in improving transverse moduli and mitigating the discontinuities of inter-laminar shear stress.

Keywords: Wave propagation; Spectral element; Multiscale hybrid composite; Graphene

1. Introduction

As a key structural element, carbon fiber-reinforced polymer (CFRP) composites are widely employed in various engineering domains, such as aerospace, marine, automotive, and building, owing to their high specific stiffness and strength [1]. With the advance of nanotechnology, modifying the polymer matrix with nanofillers has sparked extensive attention in the area of high-performance nanocomposites. Graphene platelets (GPLs) possess a high specific area with low cost, rendering them excellent candidates for the reinforcement phase. The molecular dynamic simulations and experimental measurements have demonstrated that adding a small fraction of GPLs to CFRP composites can enhance the fiber-matrix interface properties, resulting in high bonding strength and high capacity of stress transfer [2-6]. Such multiscale hybrid composites (MHCs) can find application in advanced manufacturing with the aim of providing lightweight structural designs.

Generally, the fiber-reinforced composites exhibit significant layer-wise anisotropy due to the ply orientations. By the curvature effect, shells have a great ability in resisting external loads which are prevalently used in modern industries, e.g., vehicles, rockets, branching pipelines, etc. Given the material anisotropy and complex geometries, various continuum theories, including the classical shell theory (CST) [7-9], the first-order shear deformation theory (FSDT) [10-13], and the higher-order shear deformation theory (HSDT) [14-16] were utilized to describe the constitutive behavior. Though the HSDT can achieve more realistic transverse shear strains by introducing higher-order terms, its governing equations are more complicated and the computation cost is fairly large. To alleviate the complexity of governing equations involved in the HSDT, recently developed four-variable shear deformation theories are widely used for the accurate modeling of moderately thick structures [17-26]. A notable effort has been devoted to the research on the two-phase GPL-reinforced composites (GPLRCs), while few investigations were allocated to the MHC shells [27-29]. It has been found that the high content of nanofillers tends to agglomerate, which deteriorates the resulting mechanical properties of the nanocomposite [30]. Inspired by the functionally graded (FG) materials, the concept of FG-GPL reinforced composites (FG-GPLRC) is soared in recent years [31-33]. Song et al. [34] were the first to propose the GPLRC plate where the GPLs are distributed in a stepwise manner along the thickness direction. They clarified that the mechanical properties of the GPLRC plate could be optimized by adjusting the distribution of GPLs. She and Ding [35] studied the nonlinear primary resonance of GPLRC shells with geometric imperfection. Based on the HSDT, the nonlinear bending and post-buckling of GPLRC laminates were carried out by Shen et al. [36]. They stated that the distributions of GPL play an essential

1 role in the overall behavior. Li and Han [37] analyzed the wave characteristics of piezoelectric FG-

2 GPLRC cylindrical shell with a semi-analytical formulation. For maximum use the low content of

3 GPLs, it is of significance to tailor the volume fraction of GPLs in a requisite direction to accomplish

4 the desired performance.

5 In reality, engineering structures are often experienced high-frequency loading thus inducing

6 wave propagation through them. Wave propagation analysis of composites for the development

7 of structural health monitoring has been pursued over the decades [38-45]. A number of studies

8 have been focused on the free wave propagation of MHC materials. Li et al. [46] investigated the

9 wave dispersion and band gap behavior of the periodic MHC plate. Jiang et al. [47] performed a

10 design and bandgap optimization of MHC origami-inspired metamaterials. The authors elucidated

11 that the addition of GPL reinforcements can regulate the center frequency and width of full and

12 partial band gaps. Guided waves have attracted broad interest for their ability to accurately detect

13 flaws in structures. The irregularities in the material are identified by the reflection and refraction

14 of the waves. Hence, it is crucial to consider the wave-boundary interactions, e.g., wave reflection

15 and interference, in wave propagation analysis. Such fundamental information can be acquired

16 by processing the time domain signals. However, most of the studies were restricted to dispersion

17 relations, i.e., free wave propagation. To the authors' knowledge, the literature is scarce on the

18 wave propagation in MHC materials subjected to impulse excitations. The influence of GPL on the

19 mode conversion, changes in wave velocity, and reflections has not been well understood. From

20 a mathematical view, the dynamic behavior of a mechanical system can be characterized by a

21 series of partial differential equations (PDEs), which can be tackled by analytical and numerical

22 approaches. Since the classical finite element method (FEM) becomes computationally prohibitive

23 to comply with the severe accuracy requirements for high frequency and short wavelength [48],

24 the spectral methods take the higher-order polynomials or harmonic functions as the solution

25 space to reduce the scale of spatial discretization. Azizi et al. [49] exploited the time domain

26 spectral element method to analyze the lamb wave propagation of FG plate. This method features

27 the interpolation nodes at the zeros of a set of orthogonal polynomials. On the other hand, the

28 frequency domain semi-analytical method has been popularized owing to its inherent superiority.

29 Sun and Luo [50-52] explored the wave propagation in the infinite FG plates under impact load

30 using the Laplace transform. Wang et al. [13] employed the method of reverberation ray matrix

31 (MRRM) to examine the transient responses of open laminated cylindrical shells with different

32 boundary conditions. Moreover, the frequency domain spectral element method (SEM) which

33 combines the dynamic stiffness matrix (DSM) and the fast Fourier transform (FFT) has been

34 developed to handle wave propagation problems [53]. This method retains the flexibility of FEM

1   and notably improves computational efficiency. Built upon the FSDT, Samaratunga et al. [54]
2   presented the wavelet SEM for the wave propagation in laminated plates. Nanda [55] examined
3   the dispersion relations and wave propagation behavior of laminated composite shells using the
4   SEM in the context of CST and FSDT. Abad and Rouzegar [56] established the SEM for the wave
5   propagation analysis of sandwich piezoelectric plates. Through the SEM, the dynamic responses
6   of Mindlin plates under impact and moving loads were studied by Shirmohammadi et al. [57].
7   Recently, Kim and Lee [58] extended the temporal and spatial domain SEM for the Mindlin plates
8   with consideration of arbitrary boundary conditions. Accounting for the algebraic complexity and
9   computational cost involved with HSDT in return for marginal gain in accuracy, the SEM based on
10 a theory above third order has not been attempted. The FSDT was shown to provide a balance
11 between computational efficiency and accuracy in wave propagation calculations [59]. Therefore,
12 the four-variable theory incorporating the effects of transverse shear flexibility and rotary inertia
13 would be a better option for wave propagation analysis and is the objective of the present work.

14   In this study, we develop a refined spectral element model (RSEM) to investigate the wave
15 propagation in polymer/carbon fiber/GPL composite shells. The novel aspects are as follows: (1)
16 a simple but efficient computational model is proposed to deal with the high-frequency dynamics;
17 (2) unlike previous studies were restricted to the dispersion relations, the time domain responses
18 of the structure, particularly for the wave-boundary interactions, are examined; (3) the transverse
19 reinforcing effect of graphene platelets on the shell is emphasized. Herein, the GPLs are assumed
20 to be functionally distributed along the thickness of the shell. The four-variable shear deformation
21 theory and Hamilton's principle are utilized to derive the equations of motion. The exact dynamic
22 stiffness matrix and the numerical Laplace transform are implemented to obtain the time domain
23 behavior as well as the natural frequency. The dispersion relations are studied. Furthermore, the
24 wave propagation responses for the first antisymmetric and symmetric modes are explored. A
25 parametric study is conducted to assess the elastic wave phenomena.

2. Material homogenization

27   This section specifies the geometric parameters and material constituents of the MHC shell.
28 Various distribution patterns of GPL along the thickness of the shell are considered. The volume
29 fractions of GPL vary continuously in each layer. A two-stage homogenization process is used to
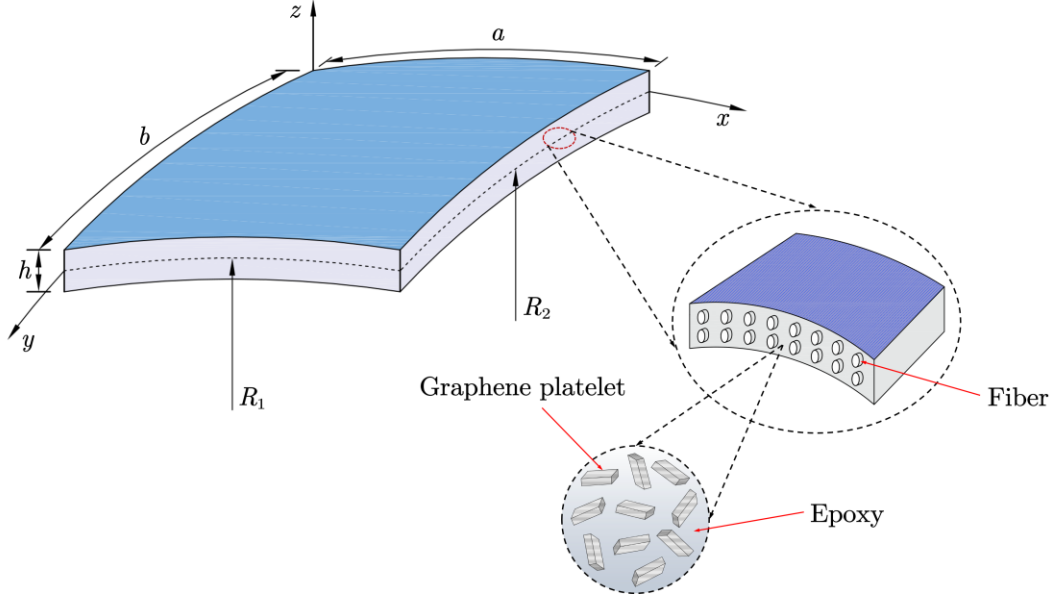30 estimate the material properties of the three-phase composite.

1

Fig. 1. Schematic of the multiscale hybrid composite shell. The shell contains multiple orthotropic layers. In the epoxy matrix space, the carbon fibers show unidirectional alignment, while the GPLs are randomly oriented and functionally distributed along the thickness.

A doubly-curved shell with length a, width b, and thickness h is illustrated in Fig. 1. A coordinate system (x,y,z) is located on the middle surface of the shell defined by $z=0$. The principal radii of curvature along x and y directions are denoted by R_1 and R_2, respectively. The composite shell consists of a mixture of epoxy matrix, carbon fibers, and graphene platelets. Typically, the nanoscale GPLs are assumed to be randomly oriented in the matrix space, and the carbon fibers are unidirectional. The fiber orientation of each layer in the shell can be tailored to produce anisotropic behavior.

A homogenization scheme is exploited to calculate the effective material properties of the three-phase composite. Firstly, based on the Halpin-Tsai micromechanical model, the Young's modulus of the GPLRC is obtained as [34, 60]

$$E_C = \frac{E_M}{8}\left[3\left(\frac{1+\lambda_1\eta_1 V_G}{1-\eta_1 V_G}\right)+5\left(\frac{1+\lambda_2\eta_2 V_G}{1-\eta_2 V_G}\right)\right] \tag{1}$$

with

$$\lambda_1 = 2l_G/t_G, \quad \lambda_2 = 2w_G/t_G \tag{2}$$

$$\eta_1 = \frac{E_G/E_M-1}{E_G/E_M+\lambda_1}, \quad \eta_2 = \frac{E_G/E_M-1}{E_G/E_M+\lambda_2} \tag{3}$$

where E_M and E_G are Young's moduli of the matrix and GPL; l_G, t_G, and w_G are average length, thickness and width of GPL, respectively; V_G is the volume fraction of GPL. Moreover, the

1   GPLs are assumed to be functionally distributed through the thickness, the volume fraction of GPL

2   for each layer is defined as

3
$$\begin{cases} U : V_G(z) = V_G^0 \\ \Lambda : V_G(z) = V_G^0(1-\vartheta) \\ X : V_G(z) = 2V_G^0|\vartheta| \\ V : V_G(z) = V_G^0(1+\vartheta) \end{cases}$$
(4)

4   in which

5
$$\vartheta = \frac{2z - (z_{k+1} + z_k)}{z_{k+1} - z_k}, \quad z_k \leq z \leq z_{k+1}$$
(5)

6   where z_k and z_{k+1} are the bottom and top z-coordinates of k th layer.

7   The total volume fraction of GPL is calculated as

8
$$V_G^0 = \frac{W_G}{W_G + (\rho_G/\rho_M)(1-W_G)}$$
(6)

9   where W_G is the weight fraction of GPL, ρ_G and ρ_M are the densities of GPL and matrix.

10   By rule of mixture, the Poisson's ratio and density of GPLRC are expressed as [34]

11
$$\nu_C = \nu_G V_G + \nu_M(1-V_G)$$
(7)

12
$$\rho_C = \rho_G V_G + \rho_M(1-V_G)$$
(8)

13 where ν_G and ν_M are the Poisson's ratios of GPL and matrix, respectively.

14   Secondly, considering the transversely isotropic carbon fibers embedded in a homogeneous

15 isotropic GPLRC, the Mori-Tanaka approach is adopted to predict the material properties of the

16 resulting composite. The effective Young's modulus E, shear modulus G, and Poisson's ratio ν

17 of the MHC shell are expressed as [61]

18
$$E_1 = V_F E_1^F + (1-V_F)E_C + 2\Upsilon_1 V_F(1-V_F)(\nu_{12}^F - \nu_C)^2$$
(9)

19
$$E_2 = \frac{E_1/(1-\nu_C^2)}{\frac{1}{1-\nu_C^2} + 2V_F\frac{E_1}{\Upsilon_2}\left[1+\nu_{23}^F - \frac{E_2^F}{E_C}(1+\nu_C)\right] + \Upsilon_1 V_F\frac{E_1^F}{E_C}\left(\frac{1+\nu_C}{E_C} - \frac{2}{E_1^F} + \frac{1-\nu_{23}^F}{E_2^F}\right)}$$
(10)

20
$$\nu_{12} = \nu_C + \frac{2\Upsilon_1 V_F}{E_C}(\nu_{12}^F - \nu_C)(1-\nu_C^2)$$
(11)

21
$$G_{12} = \frac{E_C}{2(1-V_F)(1+\nu_C)}\left\{1+V_F - 4V_F\left[1+V_F + 2(1-V_F)\frac{G_{12}^F}{E_C}(1+\nu_C)\right]^{-1}\right\}$$
(12)

1
$$G_{23} = \cfrac{E_C}{2(1+v_C)+V_F\left[\cfrac{1-V_F}{8(1-v_C^2)}+\cfrac{1}{E_C/G_{23}^F-2(1+v_C)}\right]^{-1}} \qquad (13)$$

2   with

3
$$\Upsilon_1 = \left\{-\frac{2(1-V_F)(v_{12}^F)^2}{E_1^F}+\frac{(1-V_F)(1-v_{23}^F)}{E_2^F}+\frac{(1+v_C)[1+V_F(1-2v_C)]}{E_C}\right\}^{-1} \qquad (14)$$

4
$$\Upsilon_2 = E_2^F(3+V_F-4v_C)(1+v_C)+E_C(1-V_F)(1+v_{23}^F) \qquad (15)$$

5   where V_F is the volume fraction of carbon fiber; E_1^F, E_2^F, G_{12}^F, G_{23}^F, v_{12}^F, v_{23}^F are the Young's

6   moduli, shear moduli, Poisson's ratios of carbon fiber.

7   The density of MHC shell is given as

8
$$\rho = \rho_F V_F + \rho_C(1-V_F) \qquad (16)$$

9   where ρ_F is the density of carbon fiber.

3. Theoretical framework

11   In this section, the theoretical framework of the refined spectral element model is elaborated.

12   Firstly, a simple shear deformation theory involving four variables is employed to characterize the

13   displacement field of the doubly-curved shell. The constitutive relations of an anisotropic material

14   are presented. Secondly, the equations of motion and the associated natural boundary conditions

15   are derived using the Hamilton's principle. Lastly, we implement the numerical Laplace transform,

16   and formulate the dynamic stiffness matrix according to the force-displacement relations.

3.1 Kinematics

18   On the basis of FSDT, a simplification is utilized by splitting the transverse displacement w

19   into bending, w_b, and shear components w_s, i.e., $w = w_b + w_s$ [18, 20, 62]. Such decomposition

20   for the deflection is favorable to evaluate the role of the two variables individually. The rotations

21   of transverse normal with respect to y and x axes are defined by

22
$$\phi_x = -\frac{\partial w_b}{\partial x}, \quad \phi_y = -\frac{\partial w_b}{\partial y} \qquad (17)$$

23   Following the above hypotheses, the displacement field of the doubly-curved shell can be

24   expressed as

$$u(x,y,z,t) = \left(1 + \frac{z}{R_1}\right) u_0(x,y,t) + z\phi_x(x,y,t)$$

$$v(x,y,z,t) = \left(1 + \frac{z}{R_2}\right) v_0(x,y,t) + z\phi_y(x,y,t) \tag{18}$$

$$w(x,y,z,t) = w_b(x,y,t) + w_s(x,y,t)$$

where u_0, v_0, w_b and w_s are displacement functions of the mid-plane of the shell. Clearly, the present unknowns are reduced to four as against five in FSDT. By ignoring the shear term which introduces the shear deformable effects, the theory is exactly the same as classical shell theory. Here, the approximations for a shallow shell are considered [63, 64].

The non-vanishing strain components are expressed as

$$\begin{Bmatrix} \varepsilon_x \\ \varepsilon_y \\ \gamma_{xy} \end{Bmatrix} = \begin{Bmatrix} \varepsilon_x^0 \\ \varepsilon_y^0 \\ \gamma_{xy}^0 \end{Bmatrix} + z \begin{Bmatrix} \varepsilon_x^1 \\ \varepsilon_y^1 \\ \gamma_{xy}^1 \end{Bmatrix}, \quad \begin{Bmatrix} \gamma_{xz} \\ \gamma_{yz} \end{Bmatrix} = \begin{Bmatrix} \gamma_{xz}^0 \\ \gamma_{yz}^0 \end{Bmatrix} \tag{19}$$

where

$$\begin{Bmatrix} \varepsilon_x^0 \\ \varepsilon_y^0 \\ \gamma_{xy}^0 \end{Bmatrix} = \begin{Bmatrix} \dfrac{\partial u_0}{\partial x} + \dfrac{w_b + w_s}{R_1} \\ \dfrac{\partial v_0}{\partial y} + \dfrac{w_b + w_s}{R_2} \\ \dfrac{\partial u_0}{\partial y} + \dfrac{\partial v_0}{\partial x} \end{Bmatrix}, \quad \begin{Bmatrix} \varepsilon_x^1 \\ \varepsilon_y^1 \\ \gamma_{xy}^1 \end{Bmatrix} = \begin{Bmatrix} -\dfrac{\partial^2 w_b}{\partial x^2} \\ -\dfrac{\partial^2 w_b}{\partial y^2} \\ -2\dfrac{\partial^2 w_b}{\partial x \partial y} \end{Bmatrix}, \quad \begin{Bmatrix} \gamma_{xz}^0 \\ \gamma_{yz}^0 \end{Bmatrix} = \begin{Bmatrix} \dfrac{\partial w_s}{\partial x} \\ \dfrac{\partial w_s}{\partial y} \end{Bmatrix} \tag{20}$$

For the fiber-reinforced composite, the constitutive relations are written as

$$\begin{Bmatrix} \sigma_x \\ \sigma_y \\ \sigma_{xy} \\ \sigma_{yz} \\ \sigma_{xz} \end{Bmatrix}^{(k)} = \begin{bmatrix} \bar{Q}_{11} & \bar{Q}_{12} & \bar{Q}_{16} & 0 & 0 \\ \bar{Q}_{12} & \bar{Q}_{22} & \bar{Q}_{26} & 0 & 0 \\ \bar{Q}_{16} & \bar{Q}_{26} & \bar{Q}_{66} & 0 & 0 \\ 0 & 0 & 0 & \bar{Q}_{44} & \bar{Q}_{45} \\ 0 & 0 & 0 & \bar{Q}_{45} & \bar{Q}_{55} \end{bmatrix}^{(k)} \begin{Bmatrix} \varepsilon_x \\ \varepsilon_y \\ \gamma_{xy} \\ \gamma_{yz} \\ \gamma_{xz} \end{Bmatrix} \tag{21}$$

where the transformed coefficients of stiffness, $\bar{Q}_{ij}$, are referred to Ref. [65].

3.2 Equations of motion

The equations of motion are derived using the Hamilton's principle, which is stated as

$$\int_0^T \left(\delta\Pi_s + \delta\Pi_w - \delta\Pi_k \right) dt = 0 \tag{22}$$

where $\delta\Pi_s$, $\delta\Pi_w$, and $\delta\Pi_k$ denote the variations of strain energy, work done by external forces and kinetic energy, respectively.

The variation of strain energy is

1

$$\delta\Pi_s = \int_S \int_{-h/2}^{h/2} \left(\sigma_x \delta\varepsilon_x + \sigma_y \delta\varepsilon_y + \sigma_{xy} \delta\gamma_{xy} + \sigma_{xz} \delta\gamma_{xz} + \sigma_{yz} \delta\gamma_{yz} \right) dz dS$$

$$= \int_S \left(\begin{matrix} N_x \delta\varepsilon_x^0 + N_y \delta\varepsilon_y^0 + N_{xy} \delta\gamma_{xy}^0 + M_x \delta\varepsilon_x^1 + M_y \delta\varepsilon_y^1 \\ + M_{xy} \delta\gamma_{xy}^1 + S_{xz} \delta\gamma_{xz}^0 + S_{yz} \delta\gamma_{yz}^0 \end{matrix} \right) dS \quad (23)$$

2 where the force resultants are defined by

3
$$\begin{Bmatrix} N_x \\ N_y \\ N_{xy} \end{Bmatrix} = \sum_{k=1}^N \int_{z_k}^{z_{k+1}} \begin{Bmatrix} \sigma_x \\ \sigma_y \\ \sigma_{xy} \end{Bmatrix} dz, \quad \begin{Bmatrix} M_x \\ M_y \\ M_{xy} \end{Bmatrix} = \sum_{k=1}^N \int_{z_k}^{z_{k+1}} \begin{Bmatrix} \sigma_x \\ \sigma_y \\ \sigma_{xy} \end{Bmatrix} z dz, \quad \begin{Bmatrix} S_{xz} \\ S_{yz} \end{Bmatrix} = \sum_{k=1}^N \int_{z_k}^{z_{k+1}} \begin{Bmatrix} \sigma_{xz} \\ \sigma_{yz} \end{Bmatrix} dz \quad (24)$$

4 The above force resultants can be expressed in terms of strains as

5
$$\begin{Bmatrix} N_x \\ N_y \\ N_{xy} \\ M_x \\ M_y \\ M_{xy} \end{Bmatrix} = \begin{bmatrix} A_{11} & A_{12} & A_{16} & B_{11} & B_{12} & B_{16} \\ & A_{22} & A_{26} & B_{12} & B_{22} & B_{26} \\ & & A_{66} & B_{16} & B_{26} & B_{66} \\ & & & D_{11} & D_{12} & D_{16} \\ & & & & D_{22} & D_{26} \\ sym. & & & & & D_{66} \end{bmatrix} \begin{Bmatrix} \varepsilon_x^0 \\ \varepsilon_y^0 \\ \gamma_{xy}^0 \\ \varepsilon_x^1 \\ \varepsilon_y^1 \\ \gamma_{xy}^1 \end{Bmatrix} \quad (25)$$

6
$$\begin{Bmatrix} S_{xz} \\ S_{yz} \end{Bmatrix} = \begin{bmatrix} A_{55} & A_{45} \\ A_{45} & A_{44} \end{bmatrix} \begin{Bmatrix} \gamma_{xz}^0 \\ \gamma_{yz}^0 \end{Bmatrix} \quad (26)$$

7 The stiffnesses are defined by

8
$$\left[A_{ij}, B_{ij}, D_{ij} \right] = \sum_{k=1}^N \int_{z_k}^{z_{k+1}} \bar{Q}_{ij}^{(k)} \left[1, z, z^2 \right] dz, \quad (i, j = 1, 2, 6) \quad (27)$$

9
$$\left[A_{44}, A_{45}, A_{55} \right] = \sum_{k=1}^N \int_{z_k}^{z_{k+1}} g(z) \left[\bar{Q}_{44}^{(k)}, \bar{Q}_{45}^{(k)}, \bar{Q}_{55}^{(k)} \right] dz \quad (28)$$

10 where $g(z)$ is the shear correction function, given by [66]

11
$$g(z) = \frac{5}{4} \left(1 - \frac{4z^2}{h^2} \right) \quad (29)$$

12 The work done by external force is

13
$$\delta\Pi_w = \int_S q \delta(w_b + w_s) dS \quad (30)$$

14 The variation of kinetic energy is

15
$$\delta\Pi_k = \int_S \int_{-h/2}^{h/2} \rho(z) (\dot{u}\delta\dot{u} + \dot{v}\delta\dot{v} + \dot{w}\delta\dot{w}) dz dS \quad (31)$$

16 Substituting Eq. (18) into Eq. (31), we have

1

$$\delta \Pi_k = \int_S \left\{ \begin{array}{l} I_0 \left[\dot{u}_0 \delta \dot{u}_0 + \dot{v}_0 \delta \dot{v}_0 + \left(\dot{w}_b + \dot{w}_s \right) \delta \left(\dot{w}_b + \dot{w}_s \right) \right] \\ -I_1 \left(\dfrac{\partial \dot{w}_b}{\partial x} \delta \dot{u}_0 + \dot{u}_0 \dfrac{\partial \delta \dot{w}_b}{\partial x} + \dot{v}_0 \dfrac{\partial \delta \dot{w}_b}{\partial y} + \dfrac{\partial \dot{w}_b}{\partial y} \delta \dot{v}_0 \right) \\ +I_2 \left(\dfrac{\partial \dot{w}_b}{\partial x} \dfrac{\partial \delta \dot{w}_b}{\partial x} + \dfrac{\partial \dot{w}_b}{\partial y} \dfrac{\partial \delta \dot{w}_b}{\partial y} \right) \end{array} \right\} dS \qquad (32)$$

2   where the mass inertias are

3
$$[I_0, I_1, I_2] = \sum_{k=1}^{N} \int_{z_k}^{z_{k+1}} \rho^{(k)} \left[1, z, z^2 \right] dz \qquad (33)$$

4   By combining Eqs. (23), (30) and (32), then applying the Hamilton's principle, the governing

5   equations can be expressed as

6
$$\frac{\partial N_x}{\partial x} + \frac{\partial N_{xy}}{\partial y} = I_0 \ddot{u}_0 - I_1 \frac{\partial \ddot{w}_b}{\partial x} \qquad (34)$$

7
$$\frac{\partial N_y}{\partial y} + \frac{\partial N_{xy}}{\partial x} = I_0 \ddot{v}_0 - I_1 \frac{\partial \ddot{w}_b}{\partial y} \qquad (35)$$

8
$$\frac{\partial^2 M_x}{\partial x^2} + 2 \frac{\partial^2 M_{xy}}{\partial x \partial y} + \frac{\partial^2 M_y}{\partial y^2} - \frac{N_x}{R_1} - \frac{N_y}{R_2} + q = I_0 \left(\ddot{w}_b + \ddot{w}_s \right) + I_1 \left(\frac{\partial \ddot{u}_0}{\partial x} + \frac{\partial \ddot{v}_0}{\partial y} \right) - I_2 \nabla^2 \ddot{w}_b \qquad (36)$$

9
$$\frac{\partial S_{xz}}{\partial x} + \frac{\partial S_{yz}}{\partial y} - \frac{N_x}{R_1} - \frac{N_y}{R_2} + q = I_0 \left(\ddot{w}_b + \ddot{w}_s \right) \qquad (37)$$

10   where $\nabla^2 (\cdot) = \partial^2 (\cdot) / \partial x^2 + \partial^2 (\cdot) / \partial y^2$ is the Laplace operator.

11   The associated natural boundary conditions are

12
$$\delta u_0 : N_x n_x + N_{xy} n_y \qquad (38)$$

13
$$\delta v_0 : N_y n_y + N_{xy} n_x \qquad (39)$$

14
$$\delta w_b : \frac{\partial M_n}{\partial n} + \frac{2 \partial M_{ns}}{\partial s} \qquad (40)$$

15
$$\delta w_s : S_{xz} n_x + S_{yz} n_y \qquad (41)$$

16
$$\frac{\partial \delta w_b}{\partial n} : M_n \qquad (42)$$

17   with

18
$$M_n = M_x n_x^2 + M_y n_y^2 + 2 M_{xy} n_x n_y \qquad (43)$$

19
$$M_{ns} = \left(M_y - M_x \right) n_x n_y + M_{xy} \left(n_x^2 - n_y^2 \right) \qquad (44)$$

1

$$\frac{\partial}{\partial n} = n_x \frac{\partial}{\partial x} + n_y \frac{\partial}{\partial y}, \quad \frac{\partial}{\partial s} = n_x \frac{\partial}{\partial y} - n_y \frac{\partial}{\partial x} \tag{45}$$

2 where n_x and n_y are the direction cosines of the unit normal to the middle plane.

3 For a general cross-ply laminate, the stiffness coefficients, $\overline{Q}_{16} = \overline{Q}_{26} = \overline{Q}_{45} = 0$ in Eq. (21), an

4 exact solution can be sought in Navier or Levy form. By substituting Eqs. (25) and (26) into Eqs.

5 (34)-(37), the governing equations can be further expanded in terms of displacement components,

6 which leads to lengthy expressions that are elided for brevity.

7 ## 3.3 Refined spectral element formulation

8 The spectral analysis is carried out by transforming the governing PDEs into the frequency

9 domain. To this end, the Laplace transform of a time-dependent function $f(t)$ and its inversion

10 are defined by

11

$$\mathcal{L}(\alpha + i\omega) = \int_0^\infty \left[f(t)e^{-\alpha t} \right] e^{-i\omega t} \, dt \tag{46}$$

12

$$f(t) = \frac{e^{\alpha t}}{2\pi} \int_{-\infty}^{+\infty} \mathcal{L}(\alpha + i\omega) e^{i\omega t} \, d\omega \tag{47}$$

13 where α is a real constant, ω is the circular frequency. If $\alpha = 0$, the above equations are

14 reduced to the continuous Fourier transform. It is seen that the variable α is served as a damping

15 parameter to alleviate the wraparound problem, which is typically associated with the Fourier

16 transform [67]. The Laplace transform is superior in analyzing the transient behavior of time-

17 invariant linear systems. However, the analytical Laplace transform is only valid in certain cases.

18 For the numerical implementation of Laplace transform, the efficient FFT techniques can be used

19 to perform the computation by adding an exponential window [68].

20 Considering the two opposite edges of the shell are simply supported, the displacement field

21 that satisfy the boundary conditions can be represented by the spectral form as

22

$$\begin{Bmatrix} u_0(x,y,t) \\ v_0(x,y,t) \\ w_b(x,y,t) \\ w_s(x,y,t) \end{Bmatrix} = \sum_{n=1}^{N} \sum_{m=1}^{\infty} \begin{Bmatrix} \tilde{U}_{nm} e^{-i\beta_{nm}x} \sin(\xi_m y) \\ \tilde{V}_{nm} e^{-i\beta_{nm}x} \cos(\xi_m y) \\ \tilde{W}_{nm} e^{-i\beta_{nm}x} \sin(\xi_m y) \\ \tilde{\Theta}_{nm} e^{-i\beta_{nm}x} \sin(\xi_m y) \end{Bmatrix} e^{i\omega_n t} \tag{48}$$

23 where $\tilde{U}_{nm}$, $\tilde{V}_{nm}$, $\tilde{W}_{nm}$, $\tilde{\Theta}_{nm}$ are the wave amplitudes; $i = \sqrt{-1}$ is the imaginary unit; β_{nm} is the

24 wave number, and $\xi_m = m\pi/b$ with m being the mode number. The discrete circular frequency

25 is defined as $\omega_n = 2n\pi/T$, in which T is the time window. The summation is conducted up to

1   the Nyquist frequency ω_N, where N is the number of samples in the time domain. For simplicity,

2   the subscript nm is omitted in the subsequent formulas.

3   Substituting Eq. (48) into the homogeneous governing equations ($q = 0$) yields

4

$$\begin{bmatrix} T_{11} & T_{12} & T_{13} & T_{14} \\ T_{21} & T_{22} & T_{23} & T_{24} \\ T_{31} & T_{32} & T_{33} & T_{34} \\ T_{41} & T_{42} & T_{43} & T_{44} \end{bmatrix} \begin{Bmatrix} \tilde{U} \\ \tilde{V} \\ \tilde{W} \\ \tilde{\Theta} \end{Bmatrix} = \begin{Bmatrix} 0 \\ 0 \\ 0 \\ 0 \end{Bmatrix} \tag{49}$$

5   or in matrix form as

6

$$\mathbf{Tu} = \mathbf{0} \tag{50}$$

7   where the elements $T_{ij} (i,j = 1,2,3,4)$ can be found in Appendix A.

8   For the non-trivial solution of Eq. (49), requiring the determinant $|\mathbf{T} = 0|$ leads to the tenth-

9   order polynomial of β, given by

10

$$g_5\beta^{10} + g_4\beta^8 + g_3\beta^6 + g_2\beta^4 + g_1\beta^2 + g_0 = 0 \tag{51}$$

11   where $g_j (j = 0,\ldots,5)$ are the frequency and material dependent coefficients, which are far too

12   voluminous to report. The explicit expressions can be obtained via symbolic computation using

13   the MATLAB software. Note that Eq. (51) is a fifth-order polynomial of β^2, and the roots can be

14   extracted numerically. For every frequency, there would be five pairs of wave numbers

15    $\pm\beta_j (j = 1,\ldots,5)$, corresponding to the forward and backward moving modes. Moreover, the

16   phase velocity and group velocity of wave propagation are expressed as [67]

17

$$C_p = \frac{\omega}{\text{Re}(\beta)}, \quad C_g = \frac{\mathrm{d}\omega}{\mathrm{d}\,\text{Re}(\beta)} \tag{52}$$

18   Using the obtained wave numbers, the general form of Eq. (48) can be rewritten as

19

$$\begin{Bmatrix} u_0(x,y,t) \\ v_0(x,y,t) \\ w_b(x,y,t) \\ w_s(x,y,t) \end{Bmatrix} = \sum_{n=1}^{N}\sum_{m=1}^{\infty}\sum_{j=1}^{10} \begin{Bmatrix} \tilde{U}_{nm,j}e^{-i\beta_{nm,j}x}\sin(\xi_m y) \\ \tilde{V}_{nm,j}e^{-i\beta_{nm,j}x}\cos(\xi_m y) \\ \tilde{W}_{nm,j}e^{-i\beta_{nm,j}x}\sin(\xi_m y) \\ \tilde{\Theta}_{nm,j}e^{-i\beta_{nm,j}x}\sin(\xi_m y) \end{Bmatrix} e^{i\omega_n t} \tag{53}$$

20   By setting the wave number $\beta = 0$ in Eq. (51), yields an eighth-order polynomial of ω as

21

$$k_4\omega^8 + k_3\omega^6 + k_2\omega^4 + k_1\omega^2 + k_0 = 0 \tag{54}$$

22   where $k_j (j = 0,\ldots,4)$ are dependent on the material parameters. The roots of Eq. (54) stand for

23   the cut-off frequencies at which the real wave numbers become imaginary ones [55].

1   Since the matrix $\mathbf{T}$ is singular, the spectral amplitudes are not all independent. By solving

2   for $\tilde{U}_j$, $\tilde{V}_j$ and $\tilde{\Theta}_j$ in terms of $\tilde{W}_j$, only ten unknown coefficients c_j are required. From Eq.

3   (49), the relations of the wave coefficients are defined as

4
$$\left\{\tilde{U}_j \quad \tilde{V}_j \quad \tilde{W}_j \quad \tilde{\Theta}_j\right\} = c_j\left\{r_{1,j} \quad r_{2,j} \quad 1 \quad r_{3,j}\right\}, \quad (j=1,\ldots,10) \tag{55}$$

5   For j th wave number, the amplitude ratios r_1, r_2, and r_3 can be obtained as

6
$$r_1 = \frac{\chi_1}{\chi}, \quad r_2 = \frac{\chi_2}{\chi}, \quad r_3 = \frac{\chi_3}{\chi} \tag{56}$$

7   where

8
$$\chi = \begin{vmatrix} T_{11} & T_{12} & T_{14} \\ T_{21} & T_{22} & T_{24} \\ T_{41} & T_{42} & T_{44} \end{vmatrix}, \quad \chi_1 = \begin{vmatrix} -T_{13} & T_{12} & T_{14} \\ -T_{23} & T_{22} & T_{24} \\ -T_{43} & T_{42} & T_{44} \end{vmatrix} \tag{57}$$

9
$$\chi_2 = \begin{vmatrix} T_{11} & -T_{13} & T_{14} \\ T_{21} & -T_{23} & T_{24} \\ T_{41} & -T_{43} & T_{44} \end{vmatrix}, \quad \chi_3 = \begin{vmatrix} T_{11} & T_{12} & -T_{13} \\ T_{21} & T_{22} & -T_{23} \\ T_{41} & T_{42} & -T_{43} \end{vmatrix} \tag{58}$$

10   The force-displacement relations are used to establish the DSM in the frequency domain. In

11   addition, the generalized displacements and forces are obtained from Eqs. (38)-(43). Here, a two-

12   node spectral shell element with five degrees of freedom (DOFs) per node is developed. The ten

13   nodal DOFs of the spectral shell element, at $x = 0$ and $x = L$, are

14
$$\mathbf{d} = \mathbf{\Omega c} \tag{59}$$

15   in which

16
$$\mathbf{d} = \left\{\tilde{u}_1 \quad \tilde{v}_1 \quad \tilde{w}_{b1} \quad \tilde{w}_{s1} \quad \tilde{\varphi}_1 \quad \tilde{u}_2 \quad \tilde{v}_2 \quad \tilde{w}_{b2} \quad \tilde{w}_{s2} \quad \tilde{\varphi}_2\right\}^{\mathrm{T}} \tag{60}$$

17
$$\mathbf{c} = \left\{c_1 \quad c_2 \quad \cdots \quad c_9 \quad c_{10}\right\}^{\mathrm{T}} \tag{61}$$

18   where $\tilde{u}$, $\tilde{v}$, $\tilde{w}_b$, $\tilde{w}_s$, $\tilde{\varphi}$ are the spectral form of generalized displacements, and the components

19   of the 10×10 connecting matrix $\mathbf{\Omega}$ are expressed as

20
$$\begin{aligned} &\Omega_{1,j} = r_{1,j}, \quad \Omega_{2,j} = r_{2,j}, \quad \Omega_{3,j} = 1, \quad \Omega_{4,j} = r_{3,j}, \quad \Omega_{5,j} = -i\beta_j \\ &\Omega_{6,j} = r_{1,j}e^{-i\beta_j L}, \quad \Omega_{7,j} = r_{2,j}e^{-i\beta_j L}, \quad \Omega_{8,j} = e^{-i\beta_j L}, \quad \Omega_{9,j} = r_{3,j}e^{-i\beta_j L}, \quad \Omega_{10,j} = -i\beta_j e^{-i\beta_j L} \end{aligned} \tag{62}$$
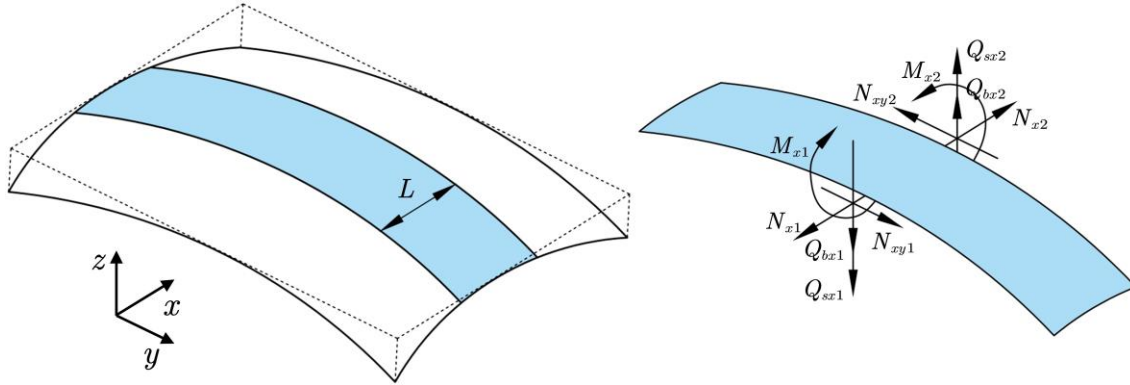
21   The nodal forces corresponding to the natural boundary conditions are expressed as

22
$$\mathbf{F} = \mathbf{\Psi c} \tag{63}$$

23   in which

24
$$\mathbf{F} = \left\{\tilde{N}_{x1} \quad \tilde{N}_{xy1} \quad \tilde{Q}_{bx1} \quad \tilde{Q}_{sx1} \quad \tilde{M}_{x1} \quad \tilde{N}_{x2} \quad \tilde{N}_{xy2} \quad \tilde{Q}_{bx2} \quad \tilde{Q}_{sx2} \quad \tilde{M}_{x2}\right\}^{\mathrm{T}} \tag{64}$$

13

where $\tilde{N}_x$, $\tilde{N}_{xy}$, $\tilde{Q}_{bx}$, $\tilde{Q}_{sx}$, $\tilde{M}_x$ are the spectral form of the generalized forces, see Fig. 2, and the components of the 10×10 connecting matrix $\mathbf{\Psi}$ are provided in Appendix B.

Fig. 2. Nodal forces and sign convention of the spectral shell element.

By combining Eqs. (59) and (63), relating the geometric boundary conditions to the natural boundary conditions, and eliminating the constant coefficients gives DSM of the shell as

$$\mathbf{S}(\omega) = \mathbf{\Psi}\mathbf{\Omega}^{-1} \tag{65}$$

The global dynamic equation is generated via the assembly process similar to the FEM, i.e.

$$\mathbf{S}_g(\omega)\mathbf{d}_g = \mathbf{F}_g \tag{66}$$

where $\mathbf{S}_g$, $\mathbf{d}_g$, and $\mathbf{F}_g$ are the global DSM, displacement vector, and force vector in frequency domain, respectively. Likewise, the force vector is generated from external loads via the virtual work principle. The algorithm of the RSEM is presented in Fig. 3. In the pre-processing step, the input force is transformed from the time domain to the frequency domain. In the post-processing step, the time domain responses are achieved by the inverse Laplace transform.

The natural frequencies can be calculated by setting the determinant of DSM to zero, i.e.

$$\left| \mathbf{S}_g(\omega) \right| = 0 \tag{67}$$

Toward this transcendental eigenvalue problem of ω, the applications of Williams-Wittrick algorithm and harmonic response curve to determine the natural frequencies can be found in Refs. [11, 69]. To elude the numerical complexities, a simple bisection method based on the sign change of determinant is employed to identify the intervals where the eigenfrequency may exist. Then the intervals can be further narrowed by varying the frequency in small steps. Repeating the iteration process enables one to acquire the results to a desired precision.
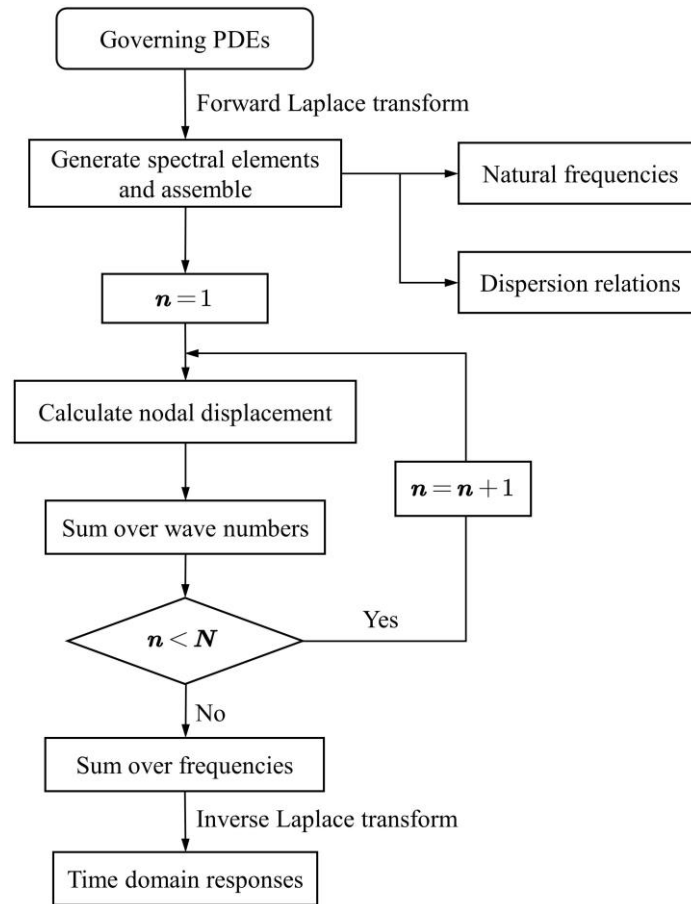
1

2   Fig. 3. Calculation procedure of the RSEM. The program involves two loops over the wave numbers

3   and frequencies.

4   For the Levy-type structures, the remaining two edges of the shell allow for the imposition

5   of arbitrary boundary conditions with the penalty method [63]. By prescribing the nodal DOFs, it

6   is able to enforce the free (F), simply supported (S) and clamped (C) boundary conditions on the

7   structure. Meanwhile, the global DSM is modified to accommodate these boundary conditions.

8   For simply supported edge, the components $\tilde{v}$, $\tilde{w}_b$, $\tilde{w}_s$ are assigned zero values; for clamped

9   edge, $\tilde{u}$, $\tilde{v}$, $\tilde{w}_b$, $\tilde{w}_s$, $\tilde{\varphi}$ are assigned zero values; for free edge, the stress resultants are assigned

10   zero values and no penalty will be applied at the generalized displacement components.

11   **4. Results and discussion**

12   In this section, we first verify the accuracy of the RSEM by comparison with published results

13   in aspects of the natural frequency and dynamic responses. Then, the RSEM is applied to the wave

14   propagation analysis of MHC shells. The main results including the dispersion relations, and time

15   domain responses are provided. The behaviors of wave dispersion, reflection, and interference,

16   are discussed. Besides, the transverse reinforcing effect of GPL on the composite is emphasized.

1   **4.1 Model verification**

2   To ensure the accuracy and reliability of the RSEM, the natural frequencies and dynamic

3   responses of laminated shells are verified by comparison with published results. In Table 1, the

4   material properties of the cross-ply laminated spherical shell are considered as [70]: $E_1 = 25E_2$,

5    $G_{12} = G_{13} = 0.5E_2$, $G_{23} = 0.2E_2$, $v_{12} = 0.25$. The non-dimensional frequency is defined as

6    $\bar{\omega} = \omega a^2 \sqrt{\rho/E_2}/h$. The natural frequencies of the shell are extracted from the DSM of Eq. (67). It

7   is observed that the present results show good agreement with those based on the HSDT for

8   different boundary conditions and radius-to-length ratios.

9

10   Table 1

11   Non-dimensional fundamental frequencies of the [0°/90°] laminated spherical shell under various

12   boundary conditions ($a/b = 1$, $a/h = 10$).

R/a	Theory	Boundary conditions					
		SSSS	SSSC	SCSC	SFSF	SFSS	SFSC
5	FSDT [55]	9.232	10.984	14.077	5.782	6.101	6.508
	HSDT [70]	9.337	11.214	14.46	5.8	6.174	6.538
	RSEM	9.2692	11.2623	14.6008	5.8114	6.1817	6.5727
20	FSDT [55]	8.921	10.638	12.714	5.767	6.091	6.534
	HSDT [70]	8.999	10.851	13.16	5.8	6.145	6.593
	RSEM	8.9242	10.9107	13.3289	5.7720	6.1505	6.5883

13

14   Afterwards, the transient vibration behavior of a [0°/90°]$_4$ laminated cylindrical shell under

15   simply supported boundary condition is examined. The geometric and material properties are

16   employed as [13]: $a = b = 1$ m , $R/a = 1$, $a/h = 10$, $E_2 = 7$ GPa , $E_1 = 15E_2$, $G_{12} = G_{13} = 0.5E_2$,

17    $G_{23} = 0.2E_2$, $v_{12} = 0.25$, $\rho = 1400$ kg/m^3 . A unit rectangular impulse with a duration of 1 ms is

18   imposed at the center of the shell, $x = 0.5$ m , $y = 0.5$ m . The time domain response of the

19   transverse displacement is measured at the point, $x = 0.75$ m , $y = 0.5$ m . For the present RSEM,

20   we adopt two spectral shell elements, 2048 sample points and a time step $\Delta t = 1 \times 10^{-5}$ s . Fig. 4

21   compares the transverse displacement of the laminated cylindrical shell calculated by RSEM and

22   the MRRM [13]. Even for this moderately thick shell, these results achieve reasonable consistency.

23   Here, the discrepancies can attribute to the shallow shell assumptions.
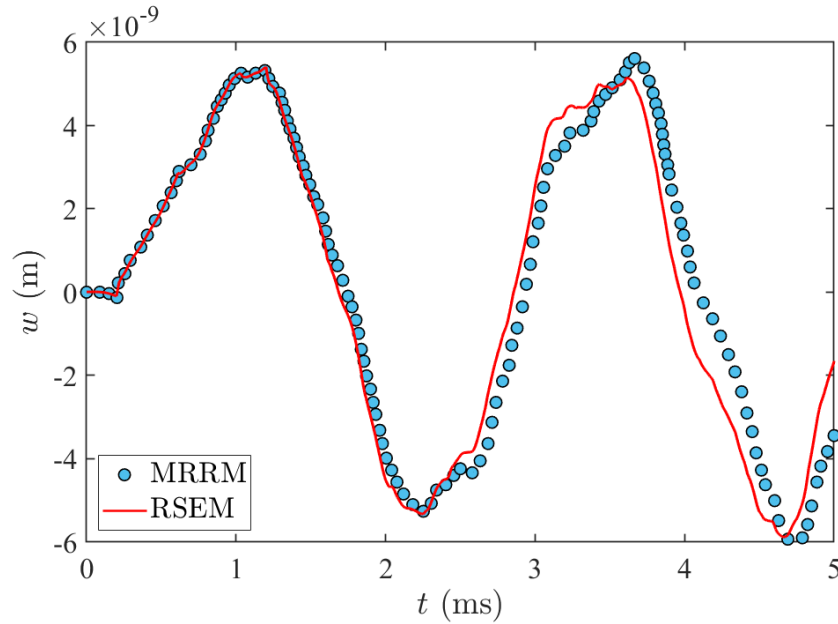
1

2 Fig. 4. Transient responses of the laminated cylindrical shell under a point impulse load. Round

3 symbol: published results. Solid line: present results.

4 **4.2 Dispersion relations**

5 The dispersion characteristics of different wave modes, such as wave number, phase velocity,

6 group velocity, are studied in this section. Unless otherwise specified, the geometric parameters

7 of the MHC shell are $h = 0.01$ m , $a/h = 50$, $a/b = 1$, $R_1 = R_2 = R$, $R/a = 1$. The lamination

8 scheme is [0°/90°/0°], the corresponding GPL distribution in each layer is adopted as $[\Lambda / X / V]$.

9 The volume fraction of carbon fiber is $V_F = 0.6$, and the weight fraction of GPL is $W_G = 1\%$. The

10 material properties of the constituents are defined as [34, 71]: carbon fiber, $E_1^F = 230$ GPa ,

11 $E_2^F = 14$ GPa , $G_{12}^F = G_{13}^F = 9$ GPa , $G_{23}^F = 5$ GPa , $v_{12}^F = 0.25$, $v_{23}^F = 0.3$, $\rho_F = 1800$ kg/m^3 ; epoxy

12 matrix, $E_M = 3$ GPa , $v_M = 0.34$, $\rho_M = 1200$ kg/m^3 ; GPL, $l_G = 2.5$ μm , $w_G = 1.5$ μm ,

13 $t_G = 1.5$ nm, $E_G = 1010$ GPa , $\rho_G = 1060$ kg/m^3 , $v_G = 0.186$.

14 Fig. 5 shows the dispersion curves of the MHC shell for different wave modes. The wave

15 numbers plotted in the negative side of the ordinate denote the imaginary part of the wave

16 numbers. The frequencies at which the imaginary wave numbers become real ones are the cut-

17 off frequencies. There are five wave modes in accord with the DOFs, i.e., out-of-plane modes w_b ,

18 w_s , and the in-plane modes u , v , as well as the flexural rotation mode $\partial w_b / \partial x$. Moreover, the

19 four cut-off frequencies corresponding to $A_0(w_b)$, $SH_0(v)$, $S_0(u)$, and $A_1(w_s)$ modes are 2.07,

20 2.40, 6.47, and 93.79 kHz. It has been found that the Lamb waves propagating in an elastic plate

1   have A_0 and S_0 fundamental branches starting from the zero frequency [72]. For the curved

2   shells, the cut-off frequencies of these branches are non-vanishing. Typically, the A_0 mode is

3   always of propagating nature, as observed from its real wave numbers. Within the low-frequency

4   region (below 6.47 kHz), the dispersion relations are more complex (see the inset in Fig. 5). These

5   wave numbers simultaneously possess real and imaginary parts, which indicates theses wave

6   modes are attenuated while propagating. Such feature gives rise to the inhomogeneous wave in

7   the shell. Beyond the fourth cut-off frequency, 93.79 kHz, the wave number of A_1 mode is

8   completely real, which means the wave starts propagating. It should be pointed out that in the

9   four-variable shear deformation theory, the wave number of flexural rotation mode $\partial w_b/\partial x$ is

10   purely imaginary, which is always evanescent in nature, as predicted by the CST [55]. The present

11   shear rotation is $\partial w_s/\partial x$, thus the A_1 mode is not corresponding to the pure shear mode.

12   Actually, the dispersion curves are highly dependent on the constitutive theory. However, the

13   present model is valid prior to the emergence of higher wave modes, and it can well capture the

14   lowest antisymmetric (A_0) and symmetric (S_0) modes. To accurately characterize the higher-

15   mode of wave propagation, the HSDT or 3D elasticity theory is required [73, 74].
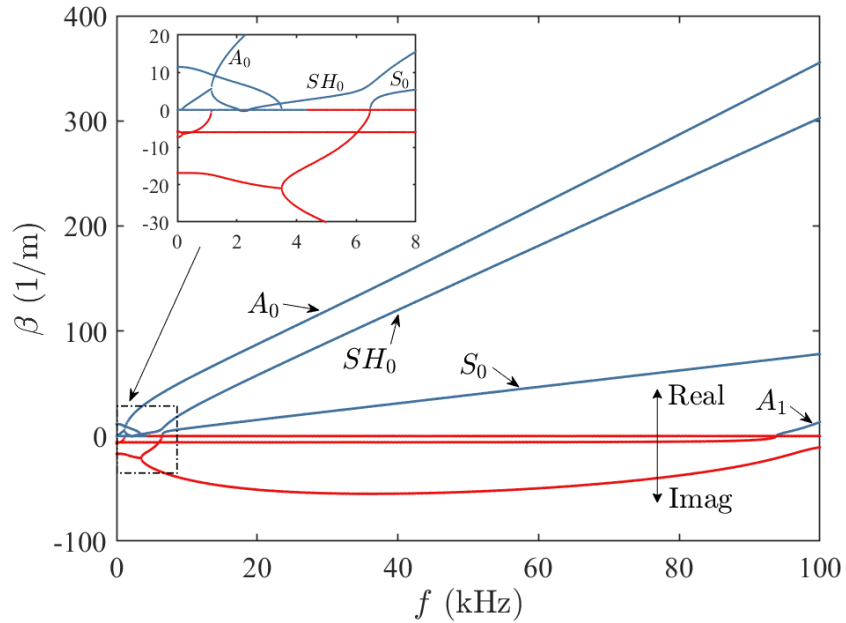
17   Fig. 5. Wave numbers versus frequency of the MHC shell. The dark blue lines and the red lines

18   denote the real and imaginary parts of the wave numbers, respectively. The inset shows the wave

19   numbers in the low frequency range.

20   Fig. 6 depicts the phase velocity and group velocity of the MHC shell for different wave

21   modes. By inspection of Eq. (52), the real parts of wave numbers are employed in calculation. As

22   discussed in Fig. 5, the waves propagate after the cut-off frequencies. The magnitude of S_0 mode

1   is much higher than the A_0 mode. Furthermore, it is concluded that all the wave modes are

2   dispersive at low frequencies, and become non-dispersive at high frequencies. Due to the

3   curvature effects, the SH_0 branch of the shell has infinite wave velocity at $\omega \to 0$. In contrast,

4   the plate-like structures have the so-called limiting velocity [75].
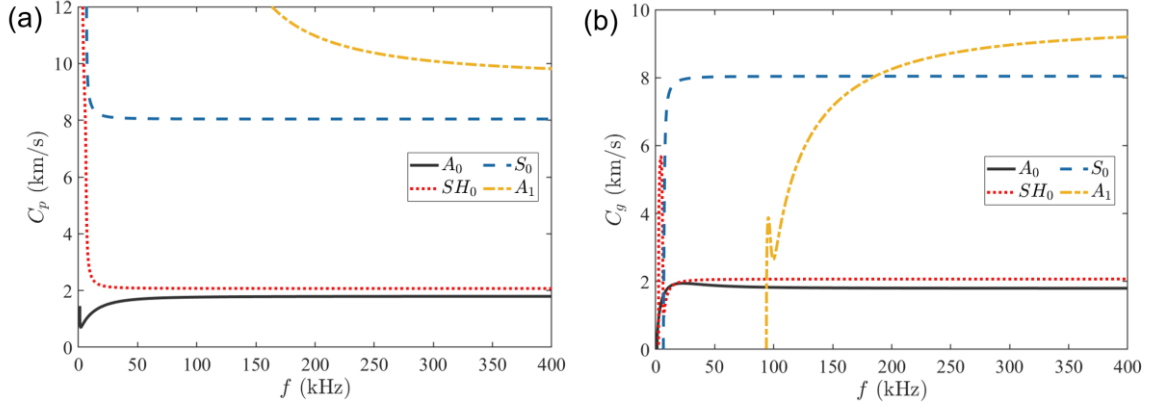
5

6   Fig. 6. Dispersion relations of the MHC shell for (a) phase velocity, and (b) group velocity.

7   The dependence of group velocity on two essential parameters is examined. Fig. 7(a) displays

8   the group velocity for A_0 mode of the MHC shell with various orthotropic ratios of carbon fiber.

9   The parameter E_2^F is specified. Three orthotropic ratios of carbon fiber are considered. The effect

10   of orthotropic ratio is remarkable at low frequencies. The largest value of orthotropic ratio yields

11   the highest group velocity. However, the dispersion curve trend is opposite at higher frequencies.

12   Fig. 7(b) shows the group velocities for A_0 wave mode of the MHC shell with various weight

13   fractions of GPL. The MHC reduces to the CFRP composite for $W_G = 0$. It is seen that the group

14   velocity of the MHC shell increases as the GPL weight fraction increases. At low frequencies (less

15   than 10 kHz), the influence of GPL weight fraction on the group velocity is quite limited, while

16   significant differences can be observed at higher frequencies. The group velocity remains constant

17   when the frequency exceeds a specific value.
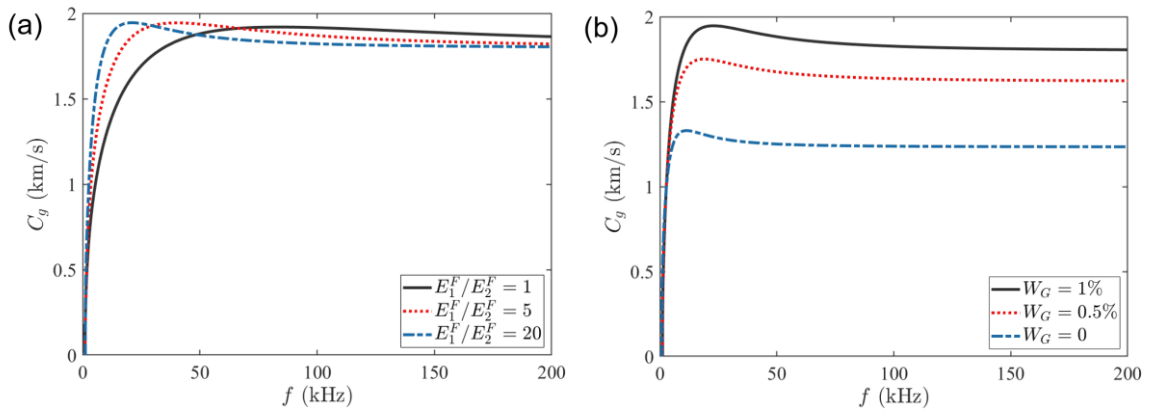
18

1   Fig. 7. Group velocity of A_0 mode in the MHC shell with the influences of (a) the orthotropic ratio

2   of carbon fiber, and (b) the weight fraction of GPL.

4.3 Wave propagation analysis

4   The dispersion relations provide the frequency domain parameters of the structure. By the

5   DSM and the numerical Laplace transform, we proceed to investigate the time domain responses

6   of the MHC shell subjected to impulsive loadings. The point impulse load is defined as

7    $$q(x,y,t) = q_0(t)\delta(x-x_0)\delta(y-y_0) \tag{68}$$

8   where $q_0(t)$ is the time-dependent force, $\delta(\cdot)$ is the Dirac delta function, x_0 and y_0 are the

9   location of the excitation point. A modulated sinusoidal load is expressed as

10    $$q_0(t) = \frac{1}{2}\left(1-\cos\frac{2\pi f_c t}{5}\right)\sin(2\pi f_c t)\left[H(t_0)-H(t_0+T_0)\right] \tag{69}$$

11   where f_c is the central frequency, $H(\cdot)$ is the Heaviside function, t_0 is the starting time, T_0 is

12   the load duration. In the calculation, 2048 sampling points are used, and the time step is chosen

13   as $\Delta t = 1\ \mu s$ with the Nyquist frequency $f_N = 500\ \text{kHz}$. In practice, though the RSEM guarantees

14   exact frequency domain solutions, errors in time domain signals due to aliasing or leakage are

15   inevitable. To remove the distortion creeps in the time histories, the damping parameter in Eq.

16   (46) is taken as equal to the frequency increment. The wave propagation responses for A_0 and

17   S_0 modes are examined.

18   Fig. 8 depicts the axial velocity of the MHC shell subjected to 50 kHz excitation. The load is

19   applied in the axial direction at the free end. The clamped-free (C-F) boundary condition along x

20   direction is considered. It is noteworthy the S_0 wave retains its wave shape while propagating.

21   This is ascribed to the non-dispersive nature of S_0 wave. The time difference is determined from

22   the peaks of two wave packets. From Fig. 8, the velocity for the S_0 mode is calculated as

23    $$C_g = \frac{2a}{t_B - t_A} = 7813\ \text{m/s} \tag{70}$$

24   According to the dispersion relations in Fig. 6(b), the group velocity for S_0 mode at 50 kHz is

25   8023 km/s, so the amount of error is 2.62%.
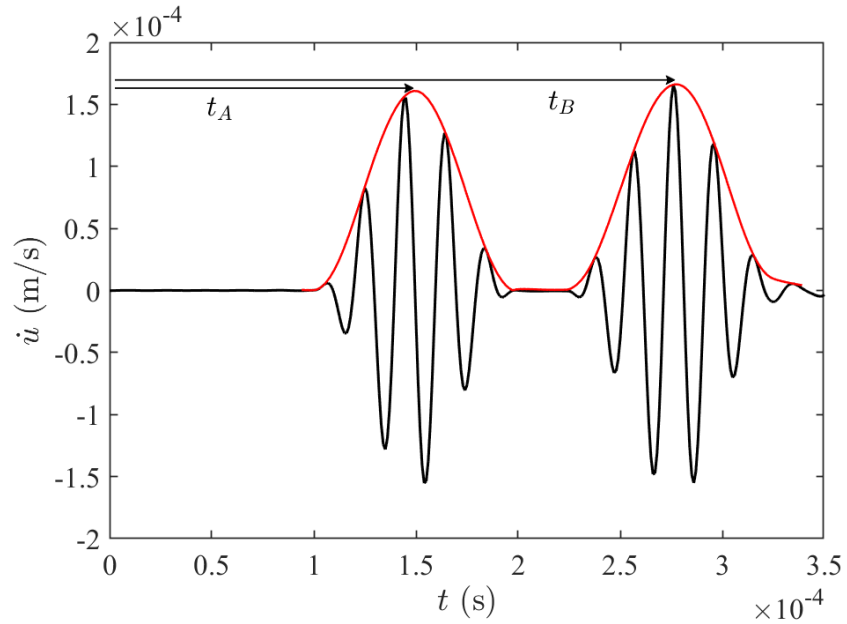
1

2   Fig. 8. Axial velocity of the MHC shell subjected to 50 kHz excitation. The envelop curve is plotted

3   to estimate the interval between the incident time, t_A, and the reflected time, t_B.

4   Fig. 9 exhibits the bending and shear parts of the transverse velocities of the MHC shell

5   subjected to 20 kHz and 50 kHz excitations, respectively. The bending part of transverse velocity

6   is larger than the shear part at low frequencies, whereas the shear part of transverse velocity is

7   predominant at higher frequencies. It is demonstrated that transverse shear has highly significant

8   effect on wave motion at high frequencies. Physically, it can be explained by the imaginary wave

9   number of the A_1 mode up to the cut-off frequency.
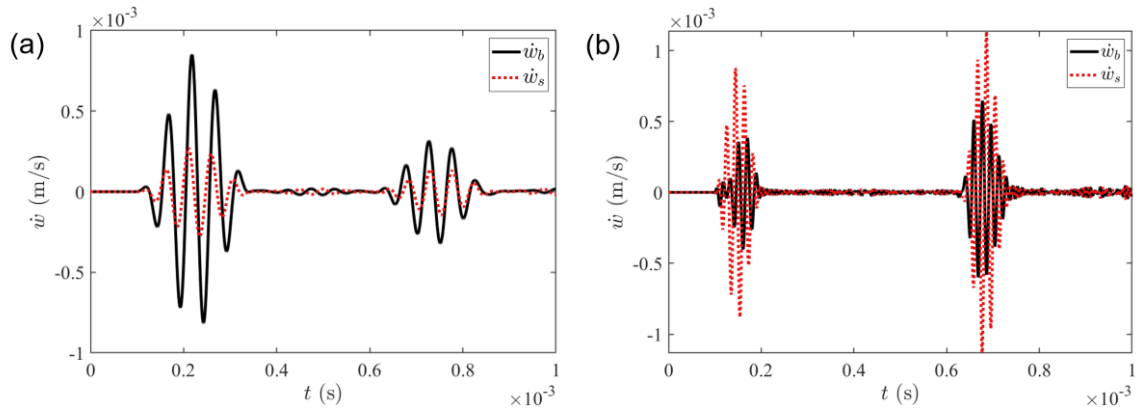
10

11   Fig. 9. Transverse velocity of the MHC shell subjected to an excitation with different central

12   frequencies: (a) 20 kHz, and (b) 50 kHz.

13   Fig. 10 illustrates the transverse velocity of the MHC shell subjected to 20 kHz excitation for

14   various orthotropic ratios of carbon fiber. The C-F boundary condition is adopted. The excitation

15   signal with a central frequency 20 kHz is applied at the middle of the free edge, and the transverse

1   velocity of the MHC shell is measured at the same point. The elastic wave propagates toward the

2   fixed end, and then multiple reflections take place. The peak of the incident wave packet is located

3   at 224 μs. Also, the time domain responses clearly indicate the arrival times of the first and second

4   reflections from the fixed end. In Fig. 10(a), the wave shape can be well maintained as the material

5   anisotropy increases. The group velocities estimated from the reflected waves and the dispersion

6   curves are shown in Fig. 10(b). Fig. 10(c) denotes the errors between the calculated values and

7   the dispersion curves in Fig. 7(a). The arrival time of first reflection matches well the dispersion

8   curves. For the case $E_1^F / E_2^F = 1$, the velocity estimated via the second reflection deviates from

9   the group velocity. In fact, the excitation wave is regarded as a narrow band one that propagates

10   almost undistorted with a velocity equal to group velocity. However, due to the wave dispersion,

11   this assumption is only accurate for ideally impulsive loading with a single frequency content.
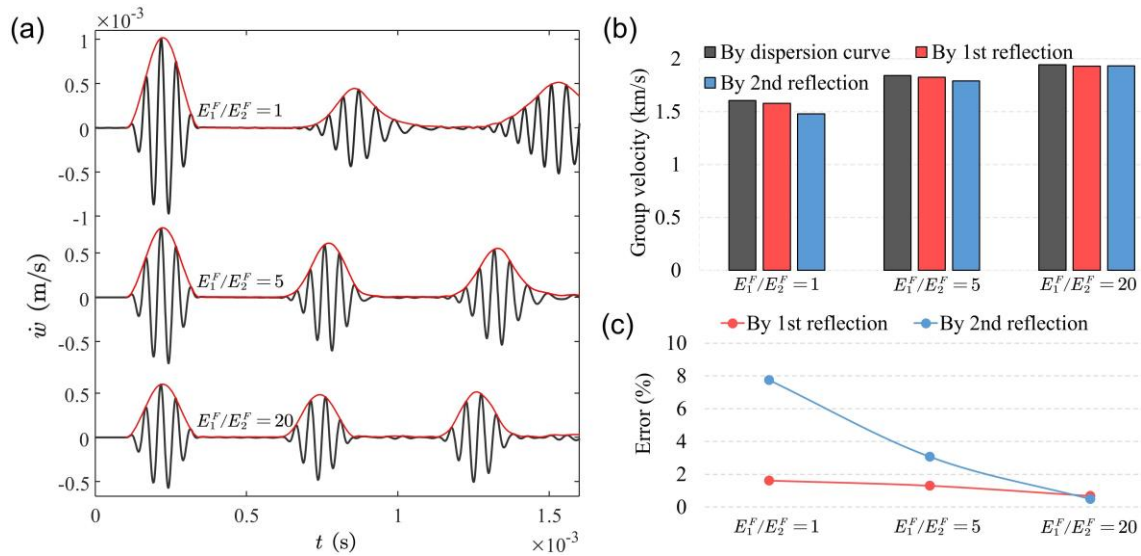
12

13   Fig. 10. Transverse velocity of the MHC shell subjected to 20 kHz excitation for various orthotropic

14   ratios of carbon fiber. (a) Time domain responses. (b) Group velocities estimated by the dispersion

15   curves and the reflected waves. (c) Errors between the dispersion curves and the estimated

16   values.

17   Fig. 11 displays the transverse velocity of the MHC shell subjected to 50 kHz excitation for

18   various weight fractions of GPL. The parameters are the same as given in Fig. 10. As shown in Fig.

19   11(a), the first peak is the incident wave and the second peak is the reflected wave from the fixed

20   end. The time differences between the two peaks are 797, 598, and 532 μs. So the propagating

21   velocities for A_0 wave mode are evaluated as 1876, 1672, and 1254 m/s, respectively. From Fig.

22   7(b), the corresponding group velocities at 50 kHz are extracted as 1882, 1675, and 1250 m/s. It

23   is found that the estimated values match well with the results, and the errors are 0.32%, 0.18%,

24   and 0.32%. It is also noted that the peak velocity decrease with the increase of weight fraction of

1   GPL. This is due to the enhanced stiffness of the composite. The propagation of A_0 wave in the

2   MHC shell at different times is shown in Fig. 11(b-e). For the cross-ply laminate, the stiffness is

3   highest in 0° and 90° directions, resulting in the highest wave velocity along them.
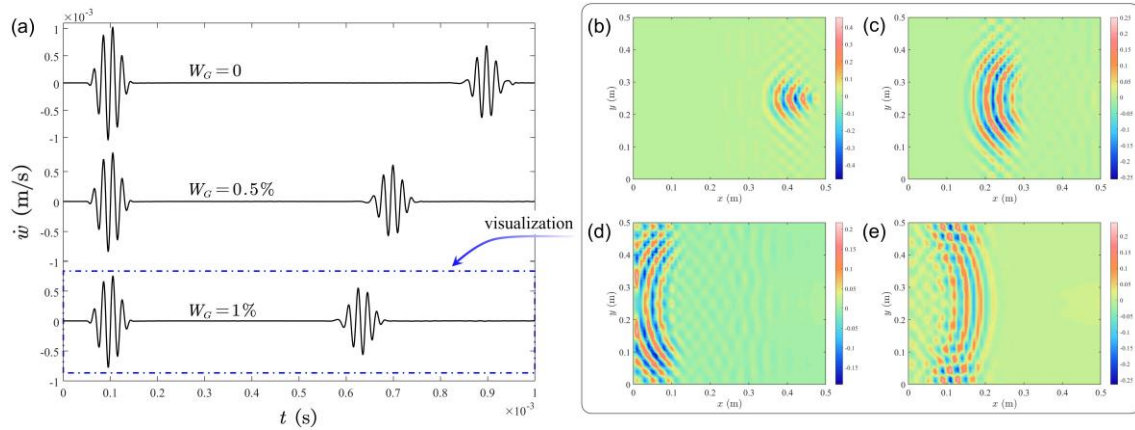

4

5   Fig. 11. Transverse velocity $\dot{w}(x,y)\times 10^{-3}$ (m/s) of the MHC shell subjected to 50 kHz excitation

6   for various weight fractions of GPL. (a) Time domain responses. (b-e) Distributions of transverse

7   velocity at different times: (b) $t = 200$ μs , (c) $t = 300$ μs , (d) $t = 400$ μs , and (e) $t = 500$ μs .

8   As aforementioned, the flexibility of the RSEM is to deal with various boundary conditions.

9   Fig. 12 represents the propagation of A_0 wave mode in the MHC shell under S-S boundary

10   conditions (simply supported at $x = 0, a$) at different times. Here, the 50 kHz excitation is applied

11   at the center of the shell, and two spectral shell elements are utilized. Clearly, the forward and

12   backward waves propagate along the x direction, which is in contrast to the individual forward

13   wave response in Fig. 11. The waves touch the boundary and then get reflected. It is noted the

14   interference of reflected waves slightly lessens the wave amplitudes.

15

1
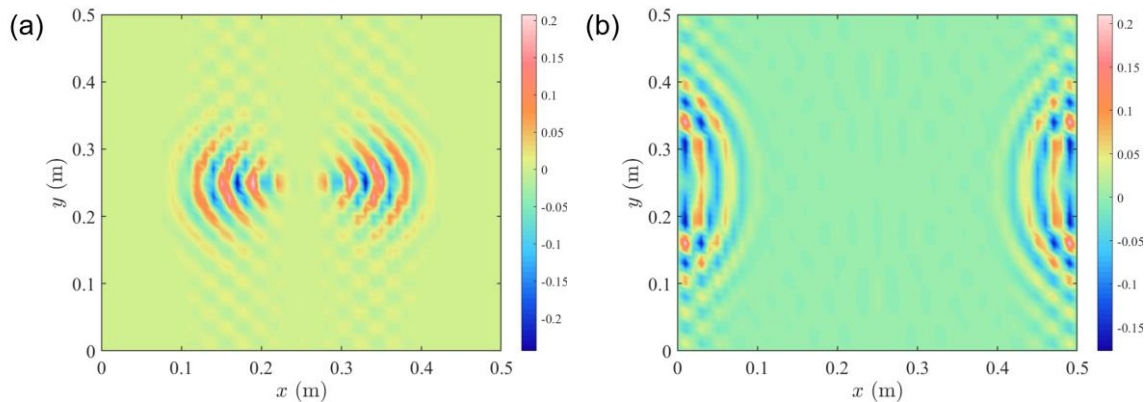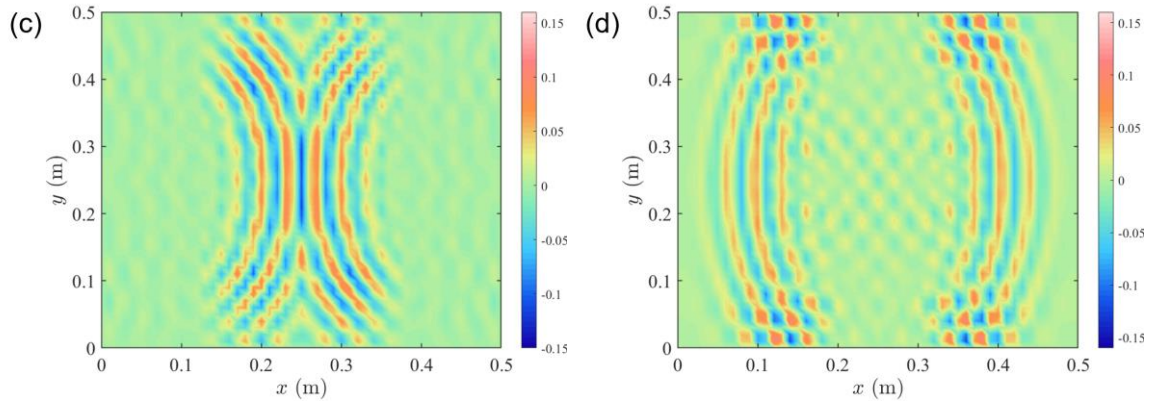
Fig. 12. Distributions of transverse velocity $\dot{w}(x,y)\times10^{-3}$ (m/s) in the MHC shell under S-S boundary condition at different times: (a) $t = 200$ μs, (b) $t = 300$ μs, (c) $t = 400$ μs, and (d) $t = 500$ μs.

In Fig. 13, we turn our attention to study the effect of GPL on the shear responses of the MHC shell under impulsive loadings. The C-F boundary condition is considered. Fig. 13(a) displays the transverse shear strain at the center of the MHC shell subjected to 50 kHz excitation. As the weight fraction of GPL increases, the peak amplitude of strain decreases. It is observed that a wavelet response appears before the larger one arrives. Since the load is applied vertically to the surface, the wave propagation in the shell is mainly in the form of A_0 wave. With the existence of wave dispersion, a small part of the S_0 wave transformed into the A_0 wave. Fig. 13(b) shows transverse shear stress along the thickness of the MHC shell at $t = 300$ μs with different GPL distributions. By varying the weight fraction of GPL in the layer, the shear moduli of the laminates can be enhanced to avoid shear failure. Experimental results also revealed that GPLs have a significant improvement on the transverse moduli [5]. In addition, the $[\Lambda/U/V]$ pattern is beneficial to alleviate the stress gap, especially under high-frequency loading. Hence, the use of GPL may allow for the minimization of the transverse reinforcing plies in the structural design, reducing the overall weight of the structure.

19
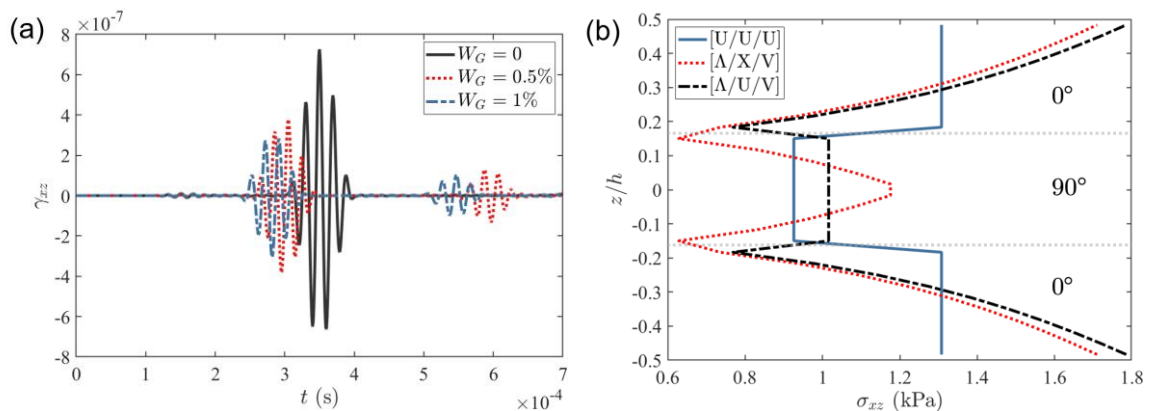
Fig. 13. Transverse shear strain and shear stress of the MHC shell subjected to 50 kHz excitation. (a) Time domain responses of transverse shear strain at the center of the shell. (b) Distribution of transverse shear stress along the thickness at $t = 300\ \mu s$ extracted from (a).

5. Concluding remarks

This paper establishes an efficient spectral element model for the wave propagation analysis of MHC shells subjected to impulsive loadings. A two-node spectral shell element with five DOFs per node is formulated. In the absence of geometric discontinuity, the transient wave responses can be exactly obtained by using only a few elements. The natural frequencies and timed domain responses are achieved by the dynamic stiffness matrix and the numerical Laplace transform. The accuracy and reliability of the RSEM are verified by the published results for laminated composite shells. In virtue of the wave number-based solutions, the RSEM can easily incorporate the parallel computing strategy. The dispersion relations indicate that the A_0 mode is always of propagating nature, while the flexural rotation mode is evanescent consistently. All the wave modes are dispersive at low frequencies and become non-dispersive with increasing frequencies. In the time domain, the velocities for A_0 and S_0 modes estimated from the wave reflections are in good agreement with the dispersion curves. It is revealed that transverse shear has highly significant effect on wave motion at high frequencies. The snapshots are plotted to visualize the reflection and interference of A_0 waves under different boundary conditions. Therein, the interference behavior caused by the reflected waves slightly lessens the wave amplitudes. Moreover, in the low-frequency range, increasing the material anisotropy diminishes the degree of wave dispersion. The inclusion of GPLs considerably enhances the transverse moduli and mitigates the discontinuities of inter-laminar shear stress, which can provide insights into lightweight structural designs.

Acknowledgments

Appendix A

$$T_{11} = A_{11}\beta^2 + A_{66}\xi^2 - I_0\omega^2$$

$$T_{12} = i\beta\xi\left(A_{12} + A_{66}\right)$$

1    $T_{13} = -i\beta\left(\beta^2 B_{11} + \xi^2\left(B_{12} + 2B_{66}\right) + \kappa_1 A_{11} + \kappa_2 A_{12} - I_1\omega^2\right)$

2    $T_{14} = -i\beta\left(\kappa_1 A_{11} + \kappa_2 A_{12}\right)$

3    $T_{21} = -T_{12}$

4    $T_{22} = A_{22}\xi^2 + A_{66}\beta^2 - I_0\omega^2$

5    $T_{23} = -\xi\left(\xi^2 B_{22} + \beta^2\left(B_{12} + 2B_{66}\right) + \kappa_1 A_{12} + \kappa_2 A_{22} - I_1\omega^2\right)$

6    $T_{24} = -\xi\left(\kappa_1 A_{12} + \kappa_2 A_{22}\right)$

7    $T_{31} = -T_{13}$

8    $T_{32} = T_{23}$

9    $T_{33} = \beta^4 D_{11} + \xi^4 D_{22} + 2\xi^2\beta^2\left(D_{12} + 2D_{66}\right) + 2\beta^2\kappa_1 B_{11} + 2\xi^2\kappa_2 B_{22} + 2B_{12}\left(\kappa_1\xi^2 + \kappa_2\beta^2\right)$
$$+ \kappa_1^2 A_{11} + 2\kappa_1\kappa_2 A_{12} + \kappa_2^2 A_{22} - \left(I_0 + I_2\left(\xi^2 + \beta^2\right)\right)\omega^2$$

10    $T_{34} = \kappa_1 B_{11}\beta^2 + \kappa_2 B_{22}\xi^2 + B_{12}\left(\kappa_1\xi^2 + \kappa_2\beta^2\right) + \kappa_1^2 A_{11} + 2\kappa_1\kappa_2 A_{12} + \kappa_2^2 A_{22} - I_0\omega^2$

11    $T_{41} = -T_{14}$

12    $T_{42} = T_{24}$

13    $T_{43} = T_{34}$

14    $T_{44} = A_{44}\xi^2 + A_{55}\beta^2 + \kappa_1^2 A_{11} + 2\kappa_1\kappa_2 A_{12} + \kappa_2^2 A_{22} - I_0\omega^2$

15   **Appendix B**

16    $\Psi_{1,j} = i\beta_j r_{1,j} A_{11} - \xi r_{2,j} A_{12} + \left(1 + r_{3,j}\right)\left(\kappa_1 A_{11} + \kappa_2 A_{12}\right) + \beta_j^2 B_{11} + \xi^2 B_{12}$

17    $\Psi_{2,j} = A_{66}\left(\xi r_{1,j} + i\beta_j r_{2,j}\right) - 2i\xi\beta_j B_{66}$

18    $\Psi_{3,j} = -\left(\beta_j^2 B_{11} + 2\xi^2 B_{66}\right)r_{1,j} - i\xi\beta_j r_{2,j}\left(B_{12} + 2B_{66}\right) + i\beta_j\left(1 + r_{3,j}\right)\left(\kappa_1 B_{11} + \kappa_2 B_{12}\right)$
$$+ i\beta_j\left(\beta_j^2 D_{11} + \xi^2 D_{12} + 4\xi^2 D_{66}\right)$$

19    $\Psi_{4,j} = iA_{55}\beta_j r_{3,j}$

20    $\Psi_{5,j} = i\beta_j r_{1,j} B_{11} - \xi r_{2,j} B_{12} + \left(1 + r_{3,j}\right)\left(\kappa_1 B_{11} + \kappa_2 B_{12}\right) + \beta_j^2 D_{11} + \xi^2 D_{12}$

21    $\Psi_{6,j} = \Psi_{1,j} e^{-i\beta_j L}$

22    $\Psi_{7,j} = \Psi_{2,j} e^{-i\beta_j L}$

23    $\Psi_{8,j} = \Psi_{3,j} e^{-i\beta_j L}$

24    $\Psi_{9,j} = \Psi_{4,j} e^{-i\beta_j L}$

1     $\Psi_{10,j} = \Psi_{5,j} e^{-i\beta_j L}$

2   where $\kappa_1 = 1/R_1$ and $\kappa_2 = 1/R_2$ signify the curvatures of the shell.
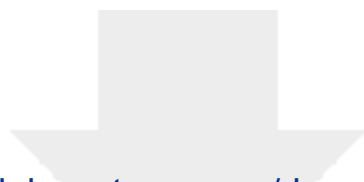
3 # References

4   [1]   Das TK, Ghosh P, Das NC. Preparation, development, outcomes, and application versatility
5   of carbon fiber-based polymer composites: a review. Adv Compos Hybrid Mater 2019;2:214-
6   33.
7   [2]   Qin W, Vautard F, Drzal LT, et al. Mechanical and electrical properties of carbon fiber
8   composites with incorporation of graphene nanoplatelets at the fiber–matrix interphase.
9   Compos Part B Eng 2015;69:335-41.
10   [3]   Cho J, Chen JY, Daniel IM. Mechanical enhancement of carbon fiber/epoxy composites by
11   graphite nanoplatelet reinforcement. Scr Mater 2007;56:685-8.
12   [4]   Aluko O, Gowtham S, Odegard GM. Multiscale modeling and analysis of graphene
13   nanoplatelet/carbon fiber/epoxy hybrid composite. Compos Part B Eng 2017;131:82-90.
14   [5]   Hadden CM, Klimek-McDonald DR, Pineda EJ, et al. Mechanical properties of graphene
15   nanoplatelet/carbon fiber/epoxy hybrid composites: Multiscale modeling and experiments.
16   Carbon 2015;95:100-12.
17   [6]   Pathak AK, Borah M, Gupta A, et al. Improved mechanical properties of carbon
18   fiber/graphene oxide-epoxy hybrid composites. Compos Sci Technol 2016;135:28-38.
19   [7]   Zeighampour H, Tadi Beni Y, Botshekanan Dehkordi M. Wave propagation in viscoelastic thin
20   cylindrical nanoshell resting on a visco-Pasternak foundation based on nonlocal strain
21   gradient theory. Thin Walled Struct 2018;122:378-86.
22   [8]   Liu Y, Hu W, Zhu R, et al. Dynamic responses of corrugated cylindrical shells subjected to
23   nonlinear low-velocity impact. Aerosp Sci Technol 2022;121:107321.
24   [9]   Bahrami S, Shirmohammadi F, Saadatpour MM. Vibration analysis of thin shallow shells
25   using spectral element method. Appl Math Modell 2017;44:470-80.
26   [10]   Bisheh H, Wu N. Wave propagation in piezoelectric cylindrical composite shells reinforced
27   with angled and randomly oriented carbon nanotubes. Compos Part B Eng 2019;160:10-30.
28   [11]   Ich Thinh T, Nguyen MC. Dynamic stiffness matrix of continuous element for vibration of
29   thick cross-ply laminated composite cylindrical shells. Compos Struct 2013;98:93-102.
30   [12]   Fu T, Wu X, Xiao Z, et al. Study on dynamic instability characteristics of functionally graded
31   material sandwich conical shells with arbitrary boundary conditions. Mech Syst Signal
32   Process 2021;151:107438.
33   [13]   Wang Q, Shao D, Qin B. A simple first-order shear deformation shell theory for vibration
34   analysis of composite laminated open cylindrical shells with general boundary conditions.
35   Compos Struct 2018;184:211-32.
36   [14]   Reddy JN, Liu CF. A higher-order shear deformation theory of laminated elastic shells. Int J
37   Eng Sci 1985;23:319-30.
38   [15]   Mantari JL, Oktem AS, Guedes Soares C. Bending and free vibration analysis of isotropic and
39   multilayered plates and shells by using a new accurate higher-order shear deformation
40   theory. Compos Part B Eng 2012;43:3348-60.
41   [16]   Karami B, Shahsavari D. On the forced resonant vibration analysis of functionally graded
42   polymer composite doubly-curved nanoshells reinforced with graphene-nanoplatelets.
43   Comput Methods Appl Mech Eng 2020;359:112767.
44   [17]   Duan Y, Zhang B, Zhang X, et al. Accurate mechanical buckling analysis of couple stress-based
45   skew thick microplates. Aerosp Sci Technol 2023;132:108056.

[18] Bourada M, Tounsi A, Houari MSA, et al. A new four-variable refined plate theory for thermal buckling analysis of functionally graded sandwich plates. J Sandwich Struct Mater 2011;14:5-33.

[19] Mantari JL, Granados EV. A refined FSDT for the static analysis of functionally graded sandwich plates. Thin Walled Struct 2015;90:150-8.

[20] Thai H-T, Kim S-E. Free vibration of laminated composite plates using two variable refined plate theory. Int J Mech Sci 2010;52:626-33.

[21] Zaoui FZ, Ouinas D, Tounsi A. New 2D and quasi-3D shear deformation theories for free vibration of functionally graded plates on elastic foundations. Compos Part B Eng 2019;159:231-47.

[22] Thai H-T, Nguyen T-K, Vo TP, et al. Analysis of functionally graded sandwich plates using a new first-order shear deformation theory. Eur J Mech A Solids 2014;45:211-25.

[23] Hua F, Fu W, You Q, et al. Wave dispersion characteristics of laminated carbon fiber reinforced polymer composite shells resting on viscoelastic foundations under thermal field. Compos Struct 2022;301:116225.

[24] Hua F, Fu W, Zhou X. Guided wave propagation in functionally graded viscoelastic polymer composite shells reinforced with graphite particles. Waves Random Complex Media 2022:1-27.

[25] Mantari JL, Guedes Soares C. Four-unknown quasi-3D shear deformation theory for advanced composite plates. Compos Struct 2014;109:231-9.

[26] Zhang B, He Y, Liu D, et al. Free vibration analysis of four-unknown shear deformable functionally graded cylindrical microshells based on the strain gradient elasticity theory. Compos Struct 2015;119:578-97.

[27] Badarloo B, Tayebikhorami S, Mirfatah SM, et al. Nonlinear forced vibration analysis of laminated composite doubly-curved shells enriched by nanocomposites incorporating foundation and thermal effects. Aerosp Sci Technol 2022;127:107717.

[28] Karimiasl M, Ebrahimi F, Mahesh V. Nonlinear forced vibration of smart multiscale sandwich composite doubly curved porous shell. Thin Walled Struct 2019;143:106152.

[29] Shahmohammadi MA, Mirfatah SM, Salehipour H, et al. Free vibration and stability of hybrid nanocomposite-reinforced shallow toroidal shells using an extended closed-form formula based on the Galerkin method. Mech Adv Mater Struct 2022;29:5284-300.

[30] Tang L-C, Wan Y-J, Yan D, et al. The effect of graphene dispersion on the mechanical properties of graphene/epoxy composites. Carbon 2013;60:16-27.

[31] Zhao S, Zhao Z, Yang Z, et al. Functionally graded graphene reinforced composite structures: A review. Eng Struct 2020;210:110339.

[32] Safarpour M, Ghabussi A, Ebrahimi F, et al. Frequency characteristics of FG-GPLRC viscoelastic thick annular plate with the aid of GDQM. Thin Walled Struct 2020;150:106683.

[33] Shen H-S, Xiang Y, Fan Y, et al. Nonlinear bending analysis of FG-GRC laminated cylindrical panels on elastic foundations in thermal environments. Compos Part B Eng 2018;141:148-57.

[34] Song M, Kitipornchai S, Yang J. Free and forced vibrations of functionally graded polymer composite plates reinforced with graphene nanoplatelets. Compos Struct 2017;159:579-88.

[35] She G-L, Ding H-X. Nonlinear primary resonance analysis of initially stressed graphene platelet reinforced metal foams doubly curved shells with geometric imperfection. Acta Mech Sin 2023;39:522392.

[36] Shen H-S, Lin F, Xiang Y. Nonlinear bending and thermal postbuckling of functionally graded graphene-reinforced composite laminated beams resting on elastic foundations. Eng Struct 2017;140:89-97.

[37] Li C, Han Q. Semi-analytical wave characteristics analysis of graphene-reinforced piezoelectric polymer nanocomposite cylindrical shells. Int J Mech Sci 2020;186:105890.

[38] Barouni AK, Saravanos DA. A layerwise semi-analytical method for modeling guided wave propagation in laminated and sandwich composite strips with induced surface excitation. Aerosp Sci Technol 2016;51:118-41.

[39] Gao W, Qin Z, Chu F. Wave propagation in functionally graded porous plates reinforced with graphene platelets. Aerosp Sci Technol 2020;102:105860.

[40] She G-L. Guided wave propagation of porous functionally graded plates: The effect of thermal loadings. J Therm Stresses 2021;44:1289-305.

[41] She G-L, Ding H-X, Zhang Y-W. Wave propagation in a FG circular plate via the physical neutral surface concept. Struct Eng Mech 2022;82:225-32.

[42] Hua F, Fu W, Zhou X. Wave propagation analysis of sandwich plates with graphite particles filled viscoelastic material core in hygrothermal environments. Compos Struct 2022;288:115380.

[43] Liu X, Karami B, Shahsavari D, et al. Elastic wave characteristics in damped laminated composite nano-scaled shells with different panel shapes. Compos Struct 2021;267:113924.

[44] Mitra M, Gopalakrishnan S. Guided wave based structural health monitoring: A review. Smart Mater Struct 2016;25:053001.

[45] Barski M, Stawiarski A. The crack detection and evaluation by elastic wave propagation in open hole structures for aerospace application. Aerosp Sci Technol 2018;81:141-56.

[46] Li C, Jiang T, Liu S, et al. Dispersion and band gaps of elastic guided waves in the multi-scale periodic composite plates. Aerosp Sci Technol 2022;124:107513.

[47] Jiang T, Han Q, Li C. Design and bandgap optimization of multi-scale composite origami-inspired metamaterials. Int J Mech Sci 2023;248:108233.

[48] Maio L, Fromme P. On ultrasound propagation in composite laminates: advances in numerical simulation. Prog Aerosp Sci 2022;129:100791.

[49] Azizi N, Saadatpour MM, Mahzoon M. Analyzing first symmetric and antisymmetric Lamb wave modes in functionally graded thick plates by using spectral plate elements. Int J Mech Sci 2019;150:484-94.

[50] Sun D, Luo S-N. Wave propagation and transient response of functionally graded material circular plates under a point impact load. Compos Part B Eng 2011;42:657-65.

[51] Sun D, Luo S-N. Wave propagation and transient response of a FGM plate under a point impact load based on higher-order shear deformation theory. Compos Struct 2011;93:1474-84.

[52] Sun D, Luo S-N. Wave propagation and transient response of a functionally graded material plate under a point impact load in thermal environments. Appl Math Modell 2012;36:444-62.

[53] Doyle JF. Wave propagation in structures: an FFT-based spectral analysis methodology. Springer; 1989.

[54] Samaratunga D, Jha R, Gopalakrishnan S. Wavelet spectral finite element for wave propagation in shear deformable laminated composite plates. Compos Struct 2014;108:341-53.

[55] Nanda N. Wave propagation analysis of laminated composite shell panels using a frequency domain spectral finite element model. Appl Math Modell 2021;89:1025-40.

[56] Abad F, Rouzegar J. Exact wave propagation analysis of moderately thick Levy-type plate with piezoelectric layers using spectral element method. Thin Walled Struct 2019;141:319-31.

[57] Shirmohammadi F, Bahrami S, Saadatpour MM, et al. Modeling wave propagation in moderately thick rectangular plates using the spectral element method. Appl Math Modell 2015;39:3481-95.

[58] Kim T, Lee U. Temporal and spatial-domain DFT-based spectral element model for the dynamic analysis of a rectangular Mindlin plate. J Sound Vib 2021;509:116220.
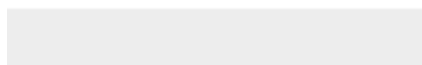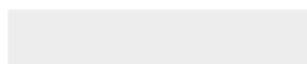
[59] Maio L, Memmolo V, Ricci F, et al. Ultrasonic wave propagation in composite laminates by numerical simulation. Compos Struct 2015;121:64-74.

[60] Rafiee MA, Rafiee J, Wang Z, et al. Enhanced mechanical properties of nanocomposites at low graphene content. ACS Nano 2009;3:3884-90.

[61] Abaimov SG, Khudyakova AA, Lomov SV. On the closed form expression of the Mori–Tanaka theory prediction for the engineering constants of a unidirectional fiber-reinforced ply. Compos Struct 2016;142:1-6.

[62] Thai H-T, Choi D-H. A simple first-order shear deformation theory for the bending and free vibration analysis of functionally graded plates. Compos Struct 2013;101:332-40.

[63] Fazzolari FA. A refined dynamic stiffness element for free vibration analysis of cross-ply laminated composite cylindrical and spherical shallow shells. Compos Part B Eng 2014;62:143-58.

[64] Aminipour H, Janghorban M, Li L. A new model for wave propagation in functionally graded anisotropic doubly-curved shells. Compos Struct 2018;190:91-111.

[65] Reddy JN. Mechanics of laminated composite plates and shells: theory and analysis. CRC Press; 2003.

[66] Civalek Ö. Free vibration of carbon nanotubes reinforced (CNTR) and functionally graded shells and plates based on FSDT via discrete singular convolution method. Compos Part B Eng 2017;111:45-59.

[67] Gopalakrishnan S. Wave propagation in materials and structures. CRC Press; 2016.

[68] Lee U. Spectral element method in structural dynamics. John Wiley & Sons; 2009.

[69] Ali MI, Azam MS, Ranjan V, et al. Free vibration of sigmoid functionally graded plates using the dynamic stiffness method and the Wittrick-Williams algorithm. Comput Struct 2021;244:106424.

[70] Khdeir AA, Reddy JN. Influence of edge conditions on the modal characteristics of cross-ply laminated shells. Comput Struct 1990;34:817-26.

[71] Dong K, Peng X, Zhang J, et al. Temperature-dependent thermal expansion behaviors of carbon fiber/epoxy plain woven composites: Experimental and numerical studies. Compos Struct 2017;176:329-41.

[72] Kuznetsov SV. Abnormal dispersion of flexural Lamb waves in functionally graded plates. Z Angew Math Phys 2019;70:89.

[73] Shoja S, Berbyuk V, Boström A. Delamination detection in composite laminates using low frequency guided waves: Numerical simulations. Compos Struct 2018;203:826-34.

[74] Yang S, Yuan FG. Transient wave propagation of isotropic plates using a higher-order plate theory. Int J Solids Struct 2005;42:4115-53.

[75] Djeran-Maigre I, Kuznetsov SV. Velocities, dispersion, and energy of SH-waves in anisotropic laminated plates. Acoust Phys 2014;60:200-7.

A refined spectral element model for wave propagation in multiscale hybrid epoxy/carbon fiber/graphene platelet composite shells

A refined spectral element model for wave propagation in multiscale hybrid epoxy/carbon fiber/graphene platelet composite shells

Declaration of interests

☒ The authors declare that they have no known competing financial interests or personal relationships that could have appeared to influence the work reported in this paper.

☐ The authors declare the following financial interests/personal relationships which may be considered as potential competing interests: